UNIVERSITY OF OKLAHOMA

GRADUATE COLLEGE

TARGETED PHOTODYNAMIC THERAPY FOR ENDOMETRIAL CANCER USING FOLIC ACID CONJUGATED GRAPHENE QUANTUM DOT-HEXAGONAL BORON NITRIDE NANOASSEMBLIES

A THESIS
SUBMITTED TO THE GRADUATE FACULTY
in partial fulfillment of the requirements for the
Degree of
MASTER OF SCIENCE

By
ABIGAIL MCCOLLUM
Norman, Oklahoma
2025

TARGETED PHOTODYNAMIC THERAPY FOR ENDOMETRIAL CANCER USING FOLIC ACID CONJUGATED GRAPHENE QUANTUM DOT-HEXAGONAL BORON NITRIDE NANOASSEMBLIES

A THESIS APPROVED FOR THE
STEPHENSON SCHOOL OF BIOMEDICAL ENGINEERING

BY THE COMMITTEE CONSISTING OF

Dr. Tahrima Rouf, Chair
Dr. John Clegg
Dr. Qinggong Tang

Table of Contents

Acknowledgments

I would like to express my thanks to my advisor, Dr. Tahrima Rouf, for her support throughout this research. I am truly grateful for the opportunities she has provided me. A special thank you to Serana Nelson, who has been both a mentor and a friend. From working together during my undergraduate research to my master's, her guidance, patience, and encouragement have meant the world to me. I truly could not have done this without her. I would also like to thank my undergraduate researchers, Ridwan, Jessica, and Krisha, for their dedication and hard work in assisting with my experiments. Your contributions were invaluable in making this research possible. I am grateful to my committee members, Dr. Qinggong Tang and Dr. John Clegg, for their support and for lending their resources. My sincere appreciation also goes to Dr. Leeza Birdwell and the LAR staff for their help with the in vivo study. I could not have done the animal study without your expertise and assistance. Thank you to Dr. Stefan Wilhelm for allowing us to use his equipment for DLS and to Dr. Michael Detamore and his lab for all the support. I also want to acknowledge the support of the SRNML staff with imaging.

Beyond my academic and research community, I owe so much to my family and friends, whose love, encouragement, and support have carried me through this journey. To my parents, thank you for always believing in me and for always being my biggest cheerleader. Mom, thank you for always being my greatest source of strength, as you have always been there to lift me up on the hard days and celebrate the good ones. Dad, thank you for always pushing me to chase my dreams. I am so grateful for the sacrifices you have made for our family. Your strength, dedication, and belief in me have kept me motivated. Zachary, thank you for always being yourself and bringing humor into my life. I am so lucky to have you as my brother. To my grandparents, thank you for always being there for me. I am forever grateful for the support you have given me

throughout my entire life. Mammy, you have always been one of my biggest inspirations, and I would not be the engineer or person I am today without you. Grandpa, thank you for always being a source of comfort, listening to me, and giving me advice whenever I come to you. To Jayci and Julianne, thank you for the pep talks, the much-needed distractions, and for always reminding me that I can achieve my goals. Ethan, words cannot express how thankful I am for you and your patience, unwavering love, and constant encouragement. You have been by my side, always reminding me that I am capable enough. I am so incredibly grateful to have you in my life. This journey has been one of the most challenging yet rewarding experiences, and I am so incredibly grateful for all those who have been on this journey alongside me.

List of Tables

List of Figures

Abstract

Endometrial cancer is the most common gynecological cancer in the United States, with current treatment options frequently being limited by a lack of specificity, increased toxicity, and moderate therapeutic efficacy. Photodynamic therapy (PDT) is a minimally invasive alternative to standard of care. PDT in the management of endometrial cancer has challenges such as oxygen dependency, poor light penetration, and biodistribution of photosensitizing agents. In this study, we developed a novel folic acid conjugated graphene quantum dot-hexagonal boron nitride (FA-GQBN) nanoassembly intended for targeted endometrial cancer PDT. GQDs were synthesized using a green, bottom-up approach using rice powder and incorporated onto hBN nanosheets to further provide stability. The nanocomposites were PEGylated to limit the aggregation and functionalized with folic acid (FA) to allow for receptor-mediated targeting of folate-receptor-positive endometrial cancer cells. Confirmation of successful synthesis, conjugation, and cellular uptake was performed using FTIR, DLS, TEM, and CLSM techniques. *In vitro* cytotoxicity studies using XTT and LDH assays confirmed the biocompatibility of FA-PEG-GQBN nanocomposites and showed inconclusive results for testing ROS. *In vivo* studies established a subcutaneous HEC1A model of an endometrial tumor. There was no detectable fluorescence of our nanoassemblies, and FA did not enhance tumor localization. Despite this, FA-GQBN nanocomposites remain a promising platform for targeted photodynamic therapy in endometrial cancer.

Chapter 1: Introduction

Overview of Endometrial Cancer

Endometrial cancer is the most common type of cancer of the female reproductive system. It forms in the endometrium, which is the inner lining of the uterus (Figure 1)[1,2]. It is expected that there will be an estimated of 69,120 new cases and 13,860 deaths in the United States in 2025[2]. The disease primarily affects postmenopausal women, with risk factors including obesity, unopposed estrogen exposure, diabetes, and Lynch syndrome[1]. Endometrial cancer is classified into Type I (estrogen-dependent, better prognosis) and Type II (estrogen-independent, more aggressive)[3]. A common symptom of endometrial cancer is abnormal uterine bleeding, which often leads to early detection and intervention[1]. While survival rates are relatively high when diagnosed early, treatment of the disease relies on a range of treatment strategies. The aim of treatment is to manage disease progression and improve patient outcomes.

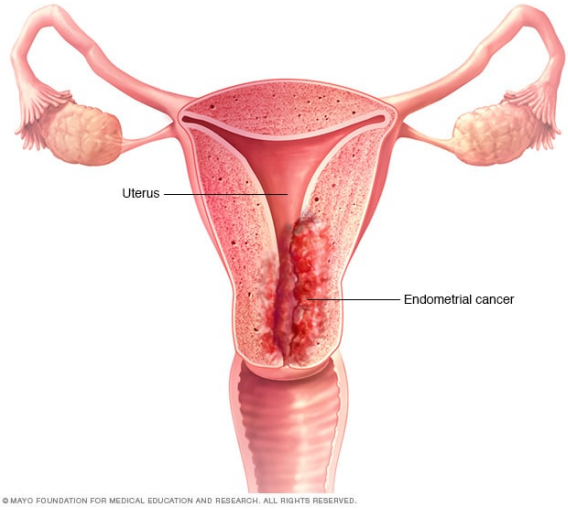

Figure 1. *Schematic of endometrial cancer in the uterus*[4].

Current Treatment Strategies

There are five standard treatments used for endometrial cancer. These include surgery, radiation therapy, chemotherapy, hormone therapy, and targeted therapy[1]. Surgery is the most common treatment for endometrial cancer. The surgical procedures to remove the endometrial cancer cells are total hysterectomy, bilateral salpingo-oophorectomy, radical hysterectomy, and lymph node dissection[1]. This is not suitable for all patients, especially for those who hope to preserve their fertility. Radiation therapy treats localized tumors and kills the cancer through high-energy X-rays[1]. This treatment option often leads to nausea, vomiting, fertility and sexual problems, hair loss, and urinary and bladder problems[5]. Chemotherapy involves drugs taken by mouth or injected into the vein or muscle to stop the growth of cancer cells[1]. When administered systemically, the chemotherapy drug can damage normal cells, causing many negative side effects. These side effects are fatigue, nausea and vomiting, loss of appetite, hair loss, and more[6]. Hormone therapy removes hormones or blocks their action to stop cancer cells from growing[1]. Targeted therapy, such as monoclonal antibody therapy, mTOR inhibitor therapy, or signal transduction inhibitor therapy, uses drugs to identify and attach to specific cancer cells, which results in less harm to normal cells than chemotherapy or radiation therapy[1]. While these treatments have shown efficacy in managing endometrial cancer, their limitations and side effects highlight the need for alternative therapeutic approaches that offer greater precision and fewer adverse effects.

Photodynamic Therapy

Photodynamic therapy (PDT) has emerged as a non-invasive treatment alternative for endometrial cancer[7]. PDT presents an organ-preserving option that could be beneficial for patients who want to preserve fertility or for those who are not surgical candidates[7]. Endoscopic access to the uterus makes PDT an ideal strategy for localized endometrial cancer treatment, offering a

minimally invasive, highly selective therapy with limited side effects[8]. However, the clinical application of PDT treatment remains limited, with most studies conducted *in vitro*, *in vivo*, *ex vivo*, and at preclinical levels[8]. Emerging research highlights the potential of PDT to be integrated with existing treatments and its role in ablating tumors while preserving healthy endometrial function[8].

PDT is a treatment that combines light energy with a photosensitizer (PS) to kill cancerous and precancerous cells[9]. PDT requires three components: photosensitizers, a light source, and oxygen dissolved in tissues[10]. The photosensitizer, a light-sensitive drug, accumulates at the tumor and can absorb specific wavelengths of light. When exposed to an appropriate wavelength of light, the PS transitions from its ground state to an excited state and then undergoes intersystem crossing to a triplet state[11]. From this state, a type I (electron transfer) or a type II (energy transfer) reaction can occur[11,12].

In type I reactions, the excited PS undergoes direct electron transfer with biomolecules in the body, such as unsaturated lipids, proteins, or nucleic acids, generating unstable radicals[11]. These unstable radicals lead to reactive oxygen species (ROS), specifically superoxide anion radical ($O_2^{\bullet -}$), a hydroxyl radical (OH•), or hydrogen peroxide (H_2O_2), which leads to oxidative damage and cytotoxicity[11]. There are two main scenarios for type I reactions. The first scenario is when electrons are transferred from the substrate to the excited triplet state of photosensitizers, which results in the formation of cationic radical substrate and anionic radical photosensitizer[13]. These radicals could then react with oxygen molecules in the environment to produce the ROS. In the second scenario, a hydrogen atom is transferred to the excited triple of the photosensitizer molecule (reduction)[13]. In type II reactions, the PS transfers energy directly to molecular oxygen to form singlet oxygen ($^1O_2$), which is a form of ROS and a highly reactive cytotoxin that plays a

major role in PDT-induced cell death[11]. The Jablonski diagram for traditional photosensitizers can be seen in Figure 2. It is believed that $^1O_2$ formed from a type II reaction is responsible for the biological PDT effect[12].

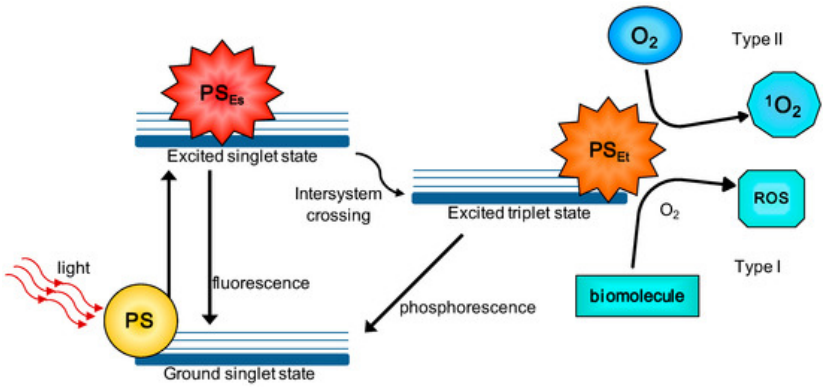

Figure 2. *Jablonski diagram for a traditional photosensitizer molecule[14].*

ROS generated through these mechanisms leads to a series of oxidative injuries that lead to various cell death pathways, including necrosis, apoptosis, necroptosis, and autophagy, based on the PS localization, light dose, and intracellular oxygen levels[10]. Necrosis, a main cell death pathway in PDT, occurs when the PS is localized at the plasma membrane, whereas apoptosis occurs when the PS accumulates in organelles such as the mitochondria, lysosomes, and endoplasmic reticulum[11]. Given the heterogeneity of endometrial tumors, optimizing PS targeting and ROS generation is crucial for maximizing PDT efficacy and minimizing off-target effects.

Despite its promise, PDT for endometrial cancer faces several challenges, including oxygen dependency, limited light penetration, and photosensitizer biodistribution[10]. Traditional PSs often suffer from poor water solubility, non-specific accumulation, and rapid clearance, limiting their therapeutic efficacy[15]. Another barrier to clinical PDT for endometrial cancer is the lack of standardized protocols, limited randomized clinical trials, and the high cost of treatment, particularly in regions where PS availability is restricted[8]. To address these challenges and

limitations, nanoparticle-based photosensitizers, such as graphene quantum dots (GQDs), have emerged as a promising alternative due to their high singlet oxygen yield, photostability, and biocompatibility. These nanomaterials offer a pathway to enhanced PS delivery, improved tumor selectivity, and deeper tissue penetration, potentially overcoming current barriers to PDT adoption in endometrial cancer treatment.

Graphene Quantum Dots

GQDs have gained attention as next-generation nanomaterials due to their unique optoelectronic properties, biocompatibility, and tunable fluorescence[16]. Since their discovery in 2008, GQDs have been used across multiple scientific disciplines, ranging from materials science to biomedical engineering[17]. Unlike bulk graphene, which has a zero bandgap, GQDs possess a non-zero bandgap due to quantum confinement and edge effects, which makes them suitable for biomedical applications[17]. This bandgap enables tunable fluorescence across a broad spectrum, including near-infrared (NIR) emission, which allows for deep-tissue imaging and optical diagnostics.

Structurally, GQDs are nanoscale graphene derivatives consisting of a single layer of sp^2-hybridized carbon sheets arranged in a hexagonal lattice[16]. The chemical structure of GQDs can be seen in Figure 3. Their electronic and optical properties are influenced by size, shape, and surface chemistry, enabling tunable fluorescence emission from the visible to NIR range. These properties make GQDs useful for fluorescence-based imaging, targeted drug delivery, and sensing[16,18]. Compared to conventional semiconductor quantum dots, which often contain toxic heavy metals, GQDs offer better biocompatibility and lower toxicity, making them safer for *in vivo* applications[16,18,19].

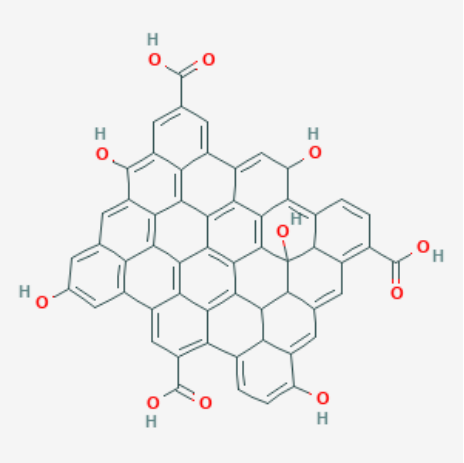

Figure 3. *Chemical structure of graphene quantum dots*[20].

The synthesis of GQDs follows two approaches: top-down and bottom-up[17,21,22]. Top-down methods involve breaking down bulk carbon materials, such as graphene, graphite, or graphene oxide (GO), into nanometer-sized fragments. These methods include chemical exfoliation, electrochemical oxidation, and hydrothermal/solvothermal treatments[22]. Using top-down methods often results in low quantum yield, poor size control, and the introduction of oxygen-containing defects that can alter the electronic structure and fluorescence properties. Bottom-up synthesis involves the controlled assembly of carbon precursors through chemical reactions such as carbonization, pyrolysis, and chemical vapor deposition. These methods allow for better control of GQD size, morphology, and surface chemistry, but could often require longer reaction times and high temperatures and yield lower product quantities than top-down approaches[17,21,22]. Top-down and bottom-up approaches are described in detail in Table 1. Purification is a major challenge in the synthesis process, as the presence of byproducts and size variations can impact their optical properties and reproducibility. Conventional synthesis methods rely on toxic solvents, strong acids, and hard oxidative reagents, which pose biological risks. To address these concerns, green synthesis strategies have started to be used more as eco-friendly alternatives[22–24]. These approaches

use biomass-derived carbon sources, such as rice powder, fruit extract, and plant waste, to produce the GQDs. Using renewable precursors not only reduces the biological risks but also allows for the introduction of heteroatom doping, like nitrogen, sulfur, or phosphorus, which can further enhance the fluorescent and electronic properties of GQDs[23]. In this study, a green-synthesis approach to fabricate GQDs from rice grains is used to produce biocompatible and fluorescent nanomaterials. This method offers an eco-friendly alternative to conventional chemical synthesis.

Table 1. Overview of top-down and bottom-up approaches to synthesizing GQDs[17,21,25].

Synthesis Method	Process	Advantages	Challenges
Top-Down Approaches			
Electrochemical Oxidation	Graphite and carbon fibers as anodes induce oxidation, forming free radicals that cut carbon sources. Electrolyte ions cleave graphene flakes into GQDs.	Environmentally friendly, mild conditions, tunable parameters, stable quality.	Complex raw material processing, low yield, produces large GQDs.

Table 2. Continued

Synthesis Method	Process	Advantages	Challenges
Top-Down Approaches			
Microwave-Assisted Exfoliation	Graphite is exfoliated using microwave radiation to provide additional heat resulting in rapid formation of high-quality GQDs.	Rapid, energy-efficient, high yield, good size control, high purity, low cytotoxicity, low cost, easy labeling.	Requires specific equipment, potential of non-uniform GQDs.
Hydrothermal/Solvothermal Method	The carbon source is oxidized and converted into GQDs under alkaline hydrothermal conditions.	Simplified process, good control over GQD size and shape, strong blue-light emission.	Requires precise temperature control, multi-step process, potential for incomplete oxidation.

Table 3. Continued

Synthesis Method	Process	Advantages	Challenges
Bottom-Up Approaches			
Carbonization/Pyrolysis	Small molecule precursors are heated above their melting point, causing condensation into GQDs.	Versatile precursor selection, tailored properties, cost-effective.	Variable quality and consistency, requires post-synthesis purification.
C_{60} Open-Cage Method	C60 fullerenes are opened with metals or acids, forming GQDs through heating and annealing.	Produces GQDs with homogeneous morphology, controlled size, and shape.	Requires precise temperature control, use of strong chemicals, complex process.
Chemical Vapor Deposition	Carbon precursors decompose on a substrate at high temperatures.	Fast synthesis speed, controllable size, good dispersion.	Requires specialized equipment, high production costs, complex.

GQDs exhibit several properties that make them ideal for biomedical applications. Their ultra-small size (1–20 nm) leads to quantum confinement effects and tunable photoluminescence, enabling size- and surface-dependent emission across the UV to NIR spectrum for high-resolution bioimaging[26,27]. Unlike traditional dyes, GQDs exhibit strong photostability and biocompatibility, making them suitable for prolonged use in live-cell imaging and tracking. Their high surface area-to-volume ratio and functional groups allow for versatile surface functionalization with drugs, targeting ligands, or therapeutic agents[22]. π– π stacking interactions with aromatic drug molecules improve drug loading and stability and enable controlled release at the tumor site[22]. Biocompatibility depends on GQD size, chemical synthesis method, and surface functionalization. GQDs that are smaller often show better cellular uptake and biodistribution, while green synthesis and PEGylation further improve safety and circulation time[16]. GQDs have been found to have minimal cytotoxicity *in vitro* and good cellular uptake. *In vivo* investigations confirm rapid renal clearance, minimal organ accumulation, and no significant systemic toxicity[19,24,28,29]. Collectively, these properties establish GQDs as a promising nanoplatform for therapies in cancer treatment.

In addition to bioimaging and drug delivery, GQDs have been shown to have potential in PDT applications. GQDs possess both photothermal and photodynamic capabilities[30,31]. When irradiated with light, they efficiently generate ROS in the form of singlet oxygen and convert light into localized heat. These capabilities make them versatile therapeutic agents. Traditional photosensitizers, like porphyrins and phthalocyanine, suffer from low $^1O_2$ quantum yields, poor photostability, and limited water stability, which restrict their clinical effectiveness[32]. GQDs have been shown to produce a $^1O_2$ yield of ~1.3, which surpasses conventional PDT efficiency[30]. This high yield contributes to a multistate sensitization (MSS) process. This means that the energy

transfer occurs from the triplet excited state to molecular oxygen, like traditional photosensitizers, and directly from the singlet excited state during the intersystem crossing[30]. GQDs can generate ROS through dual pathways under visible light irradiation because both the singlet excited state and the triplet excited state lie above the energy threshold required to convert ground-state oxygen into cytotoxic singlet oxygen[30]. This process can be seen in Figure 4. Since GQDs exhibit broad optical absorption, strong fluorescence for simultaneous imaging, and excellent biocompatibility, they can be used as next-generation PDT platforms. This study explores the potential of green-synthesized GQDs from rice grains as a sustainable and efficient photosensitizer for PDT, aiming to enhance both biocompatibility and therapeutic effectiveness.

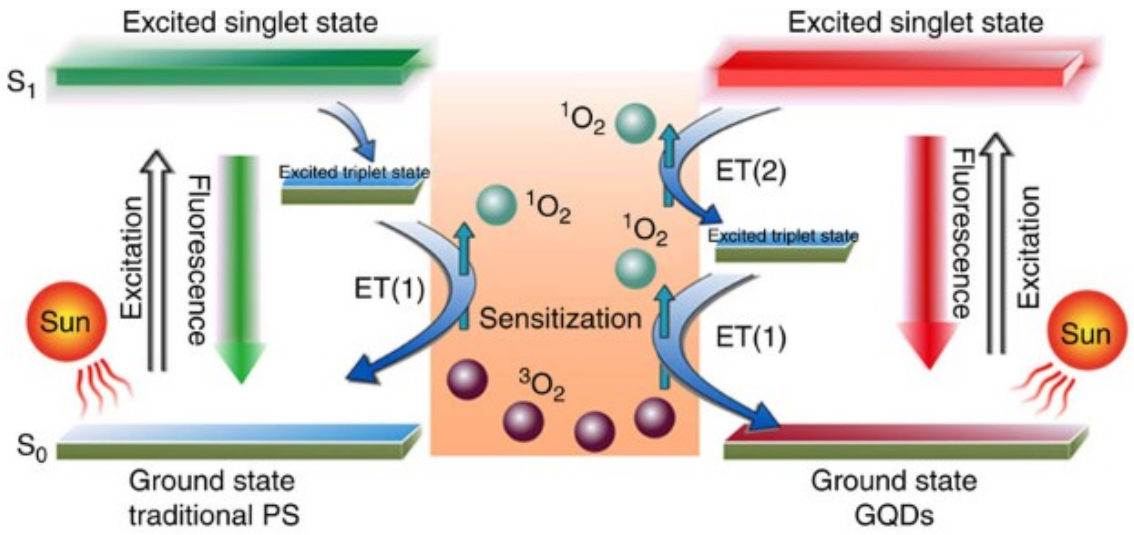

Figure 4. *Schematic of the singlet oxygen generation from traditional photosensitizers (left) and GQDs (right)[30].*

Hexagonal Boron Nitride

Despite their advantages, GQDs face challenges with stability and aqueous dispersion[17]. Their small size and high surface energy lead to aggregation, and their optical properties vary

based on defects, functional groups, and edge structures. To overcome these challenges, functionalizing GQDs with stabilizing agents, such as hexagonal boron nitride (hBN), has been explored[33,34]. hBN is a biocompatible, two-dimensional nanomaterial with a layered honeycomb-like crystalline structure, like graphene[35]. hBN is bonded by strong covalent bonds in a honeycomb configuration, with the layers attached via Van der Waals forces and oriented in a way that the boron and nitrogen atoms are placed above and below each other in adjacent layers (Figure 5)[36]. It exhibits self-assembly capabilities, high mechanical strength, excellent thermal stability, and a large electronic bandgap[35,37].

Researchers have proven that embedding GQDs into the hBN nanosheets ensures high stability, while maintaining the quantum and physiochemical properties of the GQDs[38]. The interactions between the boron and nitrogen atoms within hBN allow for its chemical inertness, oxidation resistance, and hydrophobicity. hBN also has a large electronic bandgap, which acts as an insulator to reduce charge recombination and allow the GQDs to retain their properties[35,37,38]. This makes him an ideal stabilizer for GQDs to be used in biomedical applications. hBN has a high surface area and tunable chemistry that enables functionalization with biomolecules, like targeting ligands or drugs[39]. This allows for controlled delivery and selective uptake. GQD-hBN nanocomposites (GQBN) present an opportunity to be explored further for nanomedicine applications, such as targeted photodynamic therapy.

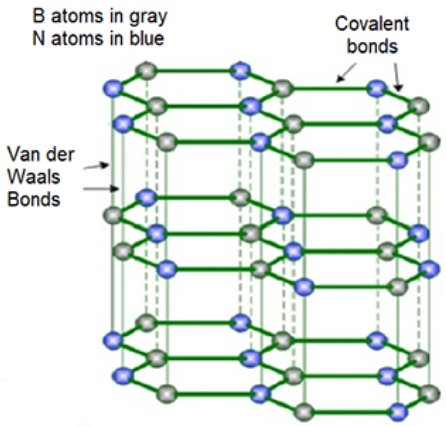

Figure 5. *Structure of boron nitride*[40].

Folic Acid Conjugated Graphene Quantum Dot-Hexagonal Boron Nitride Nanocomposites

Although GQDs and GQBN nanocomposites have started to emerge as promising nanomaterials for diverse applications, their full potential remains largely unexplored, especially in photodynamic therapy applications. One area of interest is the functionalization of GQBNs with targeting ligands that will enhance their specificity to certain receptors. Folic acid (FA) is a targeting moiety because of its high affinity for folate receptors (FR)[41]. These FRs are overexpressed on the surface of many cancer cells, particularly in gynecological cancers[42]. In endometrial carcinoma, FRα expression is significantly upregulated compared to normal endometrial tissue[43]. FA-functionalized GQBNs could serve as a nanomaterial for targeted imaging and therapy, specifically for FRα-positive gynecologic cancers.

The conjugation of folic acid to nanoparticles has been extensively studied as a strategy for enhancing tumor specificity and facilitating cellular uptake via receptor-mediated endocytosis. In previous research, FA-functionalized GQDs and FA-functionalized boron nitride nanospheres have been used for targeted cancer therapies[44–46]. Wang *et al.* showed that FA-conjugated GQDs loaded with doxorubicin (DOX), a chemotherapy drug, could selectively target HeLa cells, which

allowed for real-time monitoring of cellular uptake and drug release. In a similar study, Feng *et al.* developed folic acid-conjugated boron nitride nanospheres (BNNS) for receptor-mediated drug delivery, also using DOX. The FA functionalization enhanced cellular uptake in FRα-positive overexpressing HeLa cells. FA targeting has also been explored for PDT, not just imaging and drug delivery. A study done by Biodin *et al.* showed the feasibility of using a FA-conjugated photosensitizer in FRα-positive ovarian cancer[47]. This conjugate enhanced cellular uptake, improved phototoxicity, and reduced interleukin-6 (IL-6) secretion, which is a cytokine linked to tumor progression and chemoresistance.

In this study, we propose the development of folic acid-conjugated graphene quantum dot-hexagonal boron nitride (FA-GQBN) nanoassembly for dual-function imaging and PDT. FA-GQBNs are synthesized using an environmentally friendly and cost-effective approach. The GQDs are derived from organic short-grain white rice through a bottom-up approach. The GQBNs are functionalized with FA to allow specific and selective targeting of FR-positive cancer cells. This conjugation is expected to improve cellular uptake and tumor accumulation. This study fills gaps in the literature as FA-GQBN remains unstudied in the context of endometrial cancer PDT. We aim to address the limitations of conventional PDT by leveraging FA-GQBNs to enhance ROS generation to improve therapeutic efficacy.

Chapter 2: Scope of Thesis

Hypothesis

FA-PEG-GQBN nanoassemblies synthesized via a green, bottom-up approach will exhibit enhanced ROS generation under light irradiation due to the synergistic optical and physicochemical properties of GQDs and hBN. Conjugation with folic acid will enable receptor-mediated targeting of endometrial cancer cells, increasing cellular uptake and further amplifying ROS formation. The FA-PEG-GQBN nanoassemblies are expected to serve as effective photosensitizers for type II PDT, with strong *in vitro* and *in vivo* performance. This hypothesis will be tested by the following specific aims:

Aim 1: To optimize PEGylated GQBN fabrication with folic acid conjugation.

GQDs will be synthesized from organic rice grains using a green, bottom-up method and integrated with hBN to form GQBN nanocomposites. Polyethylene glycol (PEG) will be conjugated to improve stability, dispersion, and biocompatibility. Folic acid will be conjugated to the surface to enable the targeting of folate receptor-positive endometrial cancer cells. The resulting FA-PEG-GQBNs will be characterized for size, morphology, optical properties, and functionalization.

Aim 2: Characterize *in vitro* biocompatibility and ROS formation of FA-PEG-GQBN.

FA-PEG-GQBN nanocomposites will be evaluated *in vitro* using endometrial cancer cells to assess cytotoxicity, light-induced ROS generation, and cellular uptake. Cytotoxicity will be measured using XTT and LDH assays to evaluate metabolic activity and membrane damage, respectively. Cells treated with FA-PEG-GQBN will be irradiated with near-infrared light to assess ROS generation. These experiments will determine the biocompatibility of the nanocomposites in

the absence of light and their therapeutic potential under photoactivation. Confocal fluorescence microscopy will also be used to visualize nanoparticle internalization.

Aim 3: Evaluate the *in vivo* biodistribution and biocompatibility of GQBN and FA-PEG-GQBN nanocomposites.

Tumor-bearing mice will be used to assess the systemic behavior of FA-PEG-GQBN nanocomposites. Bioluminescent imaging will be employed to track biodistribution and tumor accumulation over time. This aim will determine the targeting specificity and circulation characteristics of FA-PEG-GQBNs, validating their potential for targeted photodynamic therapy applications.

Chapter 3: Materials and Methods

Materials

Organic short grain rice was obtained from Amazon. hBN powder was obtained from MSE Supplies LLC. Hydrochloric acid (diluted to pH 4) was borrowed from Dr. John Clegg. SteriFlip 0.22 μm filtration system was purchased from Millipore-Sigma. Molecular weight cutoff (MWCO) dialysis tubing (12-14 kDa) was obtained from Spectrum™ Labs (Fisher Scientific, USA). 1-Ethyl-3-(3-dimethylaminopropyl)carbodiimide hydrochloride Thermo Scientific. Phosphate-buffered saline, hydroxylamine, N-Hydroxysuccinimide, amine-terminated polyethylene glycol (NH_2-PEG, MW 2000), and molecular weight cutoff dialysis tubing (1000 Da) were purchased from Sigma-Aldrich. Folic acid was purchased from Thermo Scientific Chemicals (USA). HEC1A cells, McCoy's 5A culture media, fetal bovine serum, Trypsin/EDTA were purchased from ATCC (USA). The XTT Cell Viability Kit was purchased from Roche. LDH Cytotoxicity Assay Kit was obtained from Invitrogen™ (Thermo Fisher Scientific, USA). The laser supplies were borrowed from Dr. Qinggong Tang. A Thorlabs LP785-SF20 785 nm, 20 mW single-mode fiber-pigtailed laser diode, laser diode mount (LDM9LP), temperature controller (TED200C), and laser diode driver (LDC205C) were all from Thorlabs (Newton, NJ, USA).

Synthesis and Characterization

Graphene quantum dot synthesis

Twelve grams of sushi rice were weighed, washed to remove residual starches, and placed in disposable weigh boats with perforations to prevent mold growth. The weigh boat was positioned over 500 mL beakers and covered with Parafilm for two days. Once dried, the rice was ground into a fine powder using a coffee grinder. It was pulsed at high speed for eight intervals of 20 seconds each to ensure consistent size. A 500 mL beaker containing the rice powder and an

extra-large stir bar was heated to 205°C on a hot plate under constant stirring for 10 minutes. The heated rice powder was transferred to a 50 mL centrifuge tube containing 25 mL of phosphate buffer saline (PBS) and sonicated for 1 hour using a sonication bath to improve dispersion. The solution was vacuum-filtered through a 0.22 μm SteriFlip filtration system to remove larger particles. The filtered solution was placed in 12-14 kDa molecular weight cutoff (MWCO) dialysis tubing and dialyzed with diluted hydrochloric acid (pH 4) for 4 days to eliminate unreacted starch and impurities. After dialysis, the GQD solution was refiltered using a 0.22 μm Luer-lock syringe filter and transferred to 1.5 mL Eppendorf tubes for storage.

Graphene quantum dot-hexagonal boron nitride synthesis

To prepare hBN for nanocomposite synthesis, 11 mg of hBN powder was dispersed in 5 mL of phosphate-buffered saline (PBS) and subjected to bath sonication for 45 minutes to induce a positively charged surface[33]. After this, 5 mL of the GQD solution was introduced into the hBN-PBS dispersion. The electrostatic assembly of hBN and GQDs was facilitated using tip sonication at an amplitude of 30 Hz[33]. The solution underwent sonication in 30-second intervals for 5 minutes, yielding GQD-hBN (GQBN) nanocomposites.

Nanocomposite PEGylation

Carboxyl groups were activated by adding 34.5 mg of 1-ethyl-3-(3-dimethylaminopropyl)carbodiimide (EDC) and 20.7 mg of N-hydroxysuccinimide (NHS) to the GQD-hBN suspension, followed by stirring at room temperature for 30 minutes to facilitate NHS ester formation. For PEGylation, 200 mg of amine-terminated polyethylene glycol (NH_2-PEG, MW 2000) was dissolved in 1 mL of deionized (DI) water and added to the activated nanocomposite suspension. The reaction was stirred at room temperature for 4 hours to allow conjugation between NHS-activated carboxyl groups and amine-functionalized PEG molecules.

To quench any remaining active esters, 10 mM hydroxylamine (prepared by dissolving 3.475 mg of hydroxylamine in 5 mL PBS) was introduced into the reaction mixture, stirring for 30 minutes. Purification was performed using dialysis with a MWCO of 10–12 kDa, where the reaction mixture was dialyzed against PBS, pH 7.4 for 24 hours to remove unreacted reagents. The purified PEGylated nanocomposites were briefly sonicated for 5 minutes to ensure uniform dispersion and subsequently stored at 4°C for use.

Folic acid-conjugated graphene quantum dot-hexagonal boron nitride synthesis

To facilitate folic acid (FA) conjugation to GQBN nanocomposites, 2 mM FA solution was prepared by dissolving 8.83 mg of folic acid in 10 mL of PBS, pH 7.4 under gentle stirring. After, a coupling reagent solution was prepared by dissolving 24 mg of 1-ethyl-3-(3-dimethylaminopropyl)carbodiimide (EDC) and 2.87 mg of N-hydroxysuccinimide (NHS) in 3 mL of PBS. The freshly prepared EDC/NHS solution was introduced into 5 mL of GQBN suspension, and the reaction was allowed to proceed for 20 minutes at room temperature with gentle stirring to activate carboxyl groups for subsequent amide bond formation. Following activation, 1 mL of the 2 mM FA solution was added to the GQBN-EDC/NHS reaction mixture. The solution was stirred continuously for 4 hours at room temperature to enable covalent attachment of folic acid to the nanocomposite surface. To quench any remaining activated esters, 1 mM hydroxylamine solution was added to the reaction mixture and stirred for an additional 30 minutes. Purification of the FA-GQBN nanocomposites was carried out via dialysis using a 1000 MWCO membrane against PBS for 24 hours to remove unreacted reagents and byproducts. The final FA-conjugated GQBN nanocomposites were stored at 4°C for further characterization and experimentation.

Characterizations

The nanoassemblies were characterized using Fourier transform infrared spectroscopy (FTIR), dynamic light scattering (DLS), transmission electron microscopy (TEM), and confocal laser scanning microscopy (CLSM). FTIR analysis was conducted using a Thermo Scientific Nicolet iS-50 equipped with an Attenuated Total Reflection (ATR) module to confirm the presence of functional groups and verify successful conjugation. DLS measurements were conducted using a Malvern Zetasizer Nano ZS with Zetasizer software to determine the hydrodynamic size distribution of the nanocomposites in solution. TEM imaging was performed using a JEOL JEM-2010F Field Emission Transmission Electron Microscope operated at an accelerating voltage of 200 keV with a small spot size to visualize the morphology of the nanocomposites. Confocal fluorescence imaging was performed using a Leica SP8 Upright CLS/multiphoton/FLIM microscope to evaluate the fluorescence properties of the nanoassemblies and confirm their optical activity. CLSM was performed using a 63x glycerol immersion objective and 4% 405 nm UV laser power with the HyD 2 detector. Image contrast and brightness adjustments were performed using the Java-based image processing software, ImageJ.

Biological tests

XTT Cell Viability Assay

Human endometrial cancer cells (HEC1A) were seeded in 2 96-well plates 24 hours before the assay to allow for attachment. Two plates were prepared to evaluate GQD, GQBN, and FA-GQBN cytotoxicity at 3-hour and 24-hour time points. Cells were inspected under a microscope to confirm viability and confluency. Culture media (McCoy's 5A + 10% FBS), PBS, and trypsin-EDTA were pre-warmed in a bead bath before use. Adherent cells were detached by aspirating old media, washing the flask with 5 mL PBS to remove dead cells, and then adding 3 mL of trypsin.

After incubation for 5 minutes at 37°C, the reaction was neutralized with 6 mL of fresh media. The cell suspension was transferred to a 15 mL conical tube and centrifuged at 300 rcf for 3 minutes. The supernatant was removed, and the pellet was resuspended in 1 mL of fresh media, followed by an additional 1 mL to ensure uniform distribution.

Cell density was determined using an automated cell counter. A 10X dilution was prepared by mixing 80 µL of media, 20 µL of the cell suspension, and 100 µL of trypan blue stain in a 1.5 mL microcentrifuge tube. 10 µL of the mixture was loaded into the counting chamber, and live cell concentration was recorded. Cells were plated at 10,000 cells per well using a multichannel pipette. Blank wells received only media, while surrounding wells were filled with PBS to help maintain cell conditions. After seeding, plates were incubated at 37°C with 5% CO_2 overnight.

Nanoparticle (NP) solutions were prepared by diluting stock solutions in media to achieve the desired concentration (100 µg/mL) in 1.5 mL microcentrifuge tubes. All solutions were vortexed thoroughly for homogenization. Culture media was removed from wells by aspiration, and 100 µL of NP solution was added to the designated experimental wells. Control wells received fresh media. Plates were incubated for either 3 or 24 hours before proceeding to XTT addition.

The XTT kit was thawed in the dark before use. All work was performed under reduced light conditions to prevent photodegradation. Media, PBS, and XTT reagents were pre-warmed before use. Culture media was removed from experimental wells, and cells were gently washed with 150 µL of PBS per well, ensuring thorough removal of any residual NP solution. The PBS wash was aspirated, and 150 µL of the XTT reaction mixture (prepared by mixing 1.2 mL of XTT-labeling reagent with 20 µL of XTT-electron coupling reagent in 4.8 mL of media) was added to each well. The plate was incubated at 37°C for 4 hours, protected from light. After incubation, absorbance was measured using a plate reader at 450 nm, with a reference wavelength of 650 nm.

To determine cell viability, the 450 nm background absorbance was subtracted from the 650 nm absorbance before analysis before calculating percent viability using the following equation:

$$\%\, Viability = \left[\frac{Sample - Blank\ Control}{Positive\ Control}\right] * 100.$$

LDH Cytotoxicity Assay

HEC1A Cells and Nanoparticle Preparation

HEC1A cells were seeded in two 96-well plates 24 hours before the assay, one designated for laser treatment and the other for non-laser-treated cells. Cell preparation was performed following the same procedure as described in the XTT assay, including cell detachment, counting, and seeding at 10,000 cells per well. PBS was added to the surrounding wells. After seeding, plates were incubated at 37°C with 5% CO_2 overnight.

NP solutions were prepared at varying concentrations (1, 2, 5, 10, 20, 50, 100, and 200 µg/mL) by diluting stock solutions in media. All solutions were vortexed thoroughly. Culture media was removed from wells and 100 µL of each NP concentration was added to the designated experimental wells. Control wells received fresh media. Plates were incubated for 4 hours before proceeding to laser irradiation.

Laser Set-Up

A Thorlabs LP785-SF20 785 nm, 20 mW single-mode fiber-pigtailed laser diode was used for laser irradiation. The laser diode was mounted in a Thorlabs pigtailed laser diode mount (LDM9LP), which provided stable thermal management. The system was controlled using a Thorlabs TED200C temperature controller to maintain diode stability, and a Thorlabs LDC205C laser diode driver was used to regulate the laser current and power output.

The laser diode was securely positioned in the LDM9LP mount. The mount was connected to the TED200C temperature controller. The LDC205C laser diode driver was set to constant

current mode to achieve a stable output power of 20 mW at 785 nm. The laser beam was fiber-coupled and positioned over the 96-well plate using a custom alignment fixture to ensure exposure in the wells. Both well plates were washed twice with 100 uL of PBS to ensure the removal of residual nanoparticles. For the laser-treated plate, the PBS was aspirated from experimental wells, and the plate was positioned inside the laser setup. The 785 nm laser was applied for 20 seconds per well. After irradiation, fresh media was added before placing the plate back in the incubator for a 24-hour incubation period.

LDH Assay

Reagents for the LDH assay were prepared before the experiment began according to the manufacturer's information sheet. The lysis buffer, stop solution, and assay buffer stock were warmed to room temperature for 20 minutes and protected from light. The substrate stock solution was prepared by adding 11.4 mL of diH_2O to the entire substrate mix, then gently mixed. The reaction mixture was prepared by combining 600 µL of assay buffer stock solution with 11.4 mL of substrate stock solution, gently mixed, and protected from light until use. The 1X LDH positive control was prepared by diluting 1.5 µL of LDH positive control with 1 mL of 1% BSA in PBS. After 24-hour incubation, experimental samples were prepared. For spontaneous LDH activity, 10 µL of sterile ultrapure water was added to designated wells and mixed by gentle tapping. For the maximum LDH activity control, 10 µL of 10X lysis buffer was added to designated wells and mixed by gentle tapping. The plate was returned to the incubator at 37°C with 5% CO_2 for an additional 45 minutes.

After incubation, 50 µL of each sample medium (spontaneous LDH activity, maximum LDH activity, cell only, media only, and NP-treated wells) was transferred to a fresh 96-well flat-bottom plate. An optional LDH positive control assay was performed by adding 50 µL of 1X LDH

positive control to designated wells. A total of 50 µL of the prepared reaction mixture was added to each sample well, mixed by gentle tapping, and incubated at room temperature for 30 minutes, protected from light. After incubation, 50 µL of stop solution was added to each well, mixed by gentle tapping, and any bubbles were removed using a pipette tip to ensure accurate absorbance readings.

Absorbance was measured at 490 nm with a reference wavelength of 680 nm. To determine LDH activity, the 680 nm background absorbance was subtracted from the 490 nm absorbance before calculating percent cytotoxicity using the following equation:

$$\%\ Cytotoxicity = \left[\frac{Experimental\ LDH\ activity - Spontanous\ LDH\ activity}{Maximum\ LDH\ activity - Spontanous\ LDH\ acticity}\right] * 100.$$

***In Vivo* Biodistribution**

All animal studies were conducted in accordance with the institutional IACUC-approved protocol. Female Balb/c Nude mice (5–6 weeks old) were obtained from Charles River Laboratories. Subcutaneous endometrial tumor models were established by injecting 0.2 mL of a human HEC1A cell suspension ($2.5x10^7$ cells/mL, 0.2 mL) into the right flank of each mouse using a 22–25-gauge needle. Tumor growth was monitored using calipers until the volume reached approximately 140–160 mm^3. For the biodistribution study, mice were divided into three groups: (1) untreated control, (2) non-targeting PEG-GQBN-treated, and (3) targeting FA-PEG-GQBN-treated. Both nanoparticle formulations were administered as a single intravenous injection via the tail vein at a dose of 15 mg/kg in a volume of 130 µL. Nanocomposites were not externally labeled. Whole-body fluorescence imaging was performed at 1, 4, 8-, 24-, 48-, and 120-hours post-injection using the PerkinElmer IVIS Spectrum CT system. Mice were anesthetized with 1–3% isoflurane during imaging and positioned on the system's built-in stage. Fluorescence intensity within regions of interest was quantified. At the final imaging time point (120 hours), animals were euthanized

via CO_2 asphyxiation while under anesthesia. All handling, injections, and imaging procedures were performed under biosafety conditions and adhered to standard operating protocols for working with nanomaterials and biohazardous cell lines.

Statistical Analysis

Statistical analysis was performed using GraphPad Prism 10 (GraphPad Software, Inc., La Jolla, CA, USA). The statistical analysis is described in each figure legend. Data are presented as mean values ± standard deviation (SD). If $p>0.05$, the results are not statistically different. Differences were statistically significant when $*p<0.05$, $**p<0.01$, $***p<0.001$, and $****p<0.0001$.

Chapter 4: Results and Discussion

Synthesis and Characterization

The GQDs were prepared via a bottom-up, green synthesis method using rice powder. Rice powder contains starches in the form of amylose and amylopectin[48]. The heating process causes the thermal breakdown of the starches, which leads to the formation of glucose oligomers[48]. When heated at high temperatures (200°C), nucleation will take place, and pyrolysis of the glucose molecules leads to the growth of the GQDs[48]. The GQDs were then embedded onto the hBN nanosheets through electrostatic interactions[33]. The synthesized GQDs, GQBN, PEG-GQBN, and FA-PEG-GQBN can be seen in Figure 6. Various analytical techniques were employed to confirm successful synthesis and conjugation. Now, the structural characterization of these assemblies will be discussed using FTIR, DLS, TEM, and CLSM.

Figure 6. *Photograph of (from left to right) GQDs, GQBN, PEG-GQBN, and FA-PEG-GQBN.*

FTIR

To confirm the successful conjugation of the elements in the FA-GQBN nanoassembly, FTIR was performed. The FTIR results for GQDs, hBN, GQBN, FA, and FA-GQBN are shown

in Figure 7. The GQD spectrum (Figure 7a) exhibits a broad -OH peak at 3420 cm^{-1}, C=O stretching peak at 1660 cm^{-1}, and C-O stretching peak at 1080 cm^{-1} [33]. The hBN powder spectrum (Figure 7b) has characteristic peaks at 1330 cm^{-1} and 758 cm^{-1}, which correspond to -BN and B-N-B, respectively[34]. The GQBN spectrum (Figure 7c) has peaks at 3350 cm^{-1} (-OH), 1670 cm^{-1} (C=O), 1390 cm^{-1} (B-N), 1100 cm^{-1} (C-O), and 796 cm^{-1} (B-N-B)[33]. This confirms that there was successful conjugation between the GQDs and hBN. The spectrum of FA powder (Figure 7d) presents characteristic peaks at 1695 cm^{-1} (C=O), 1605 cm^{-1} (C=C), 1484 cm^{-1} (C-H)[49]. In the FA-GQBN spectrum (Figure 7e), peaks at 3390 cm^{-1} (-OH), 1640 cm^{-1} (C=O), 1410 cm^{-1} (C-H), 1090 cm^{-1} (C-O), and 994 cm^{-1} (B-N-B), confirming successful conjugation of folic acid to the GQBN[33,49].

During size optimization, filtration through a 0.22 μm Luer-lock syringe filter was explored as an option to reduce the size of the FA-GQBN nanoassemblies. After filtration of the FA-GQBN, an FTIR spectrum was taken to confirm it still contained the characteristic peaks of each element (Figure 7f). While it had all the same peaks as pre-filtration, it was missing the 1410 cm^{-1} (C-H) peak. This absent peak suggests that filtration may have removed components containing C-H bonds, possibly due to the loss of folic acid molecules. As a result, filtration was ruled out as a viable method for size optimization.

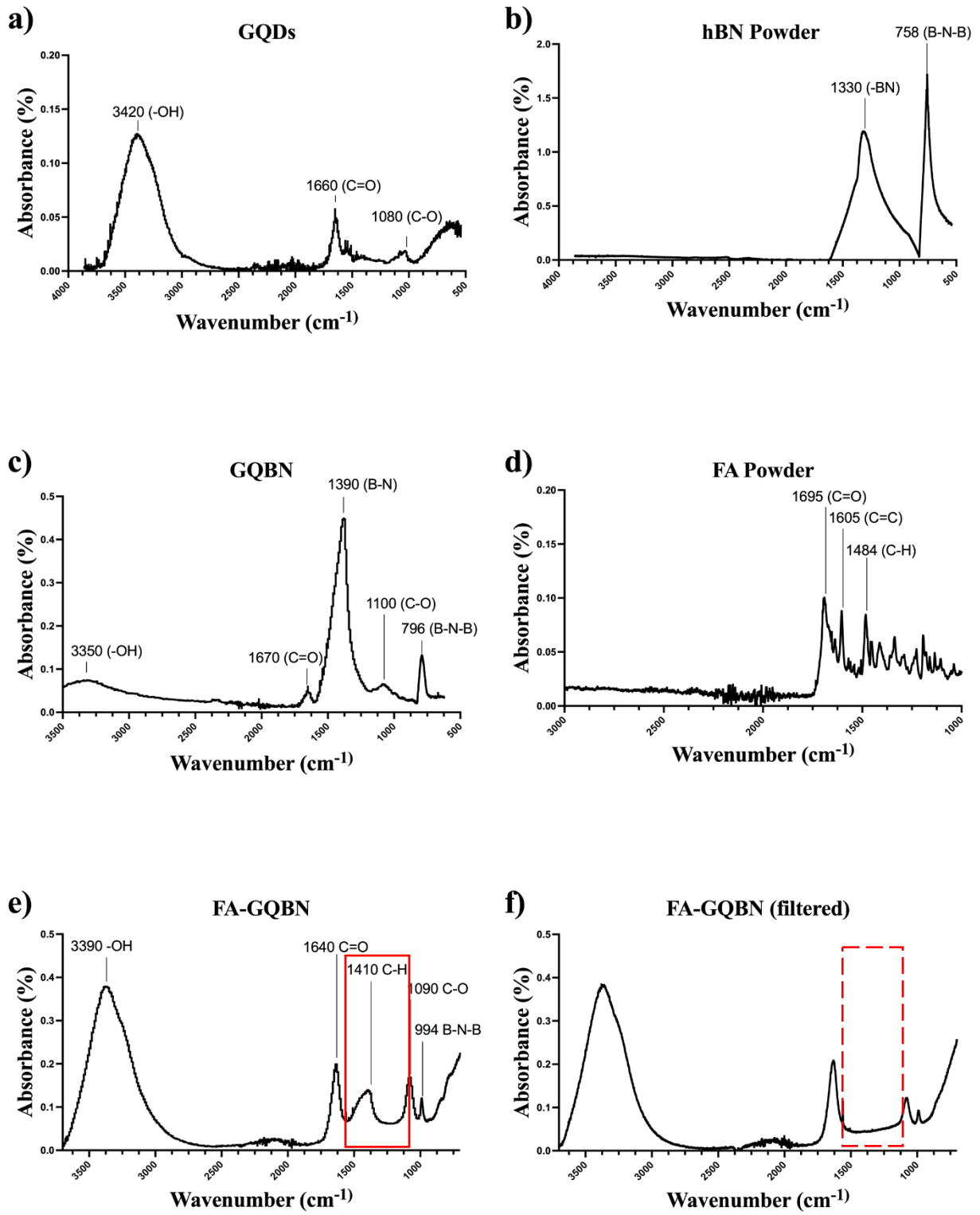

Figure 7. *FTIR Data of a) GQDs, b) hBN powder, c) GQBN, d) FA powder, e) FA-GQBN, and f) filtered FA-GQBN.*

DLS

The nanoassembly synthesis was also verified by size measurements using DLS (Figure 8). Size optimization was critical to developing the FA-GQBN nano assemblies, as controlling the particle size impacts their stability and cellular uptake. DLS was performed after each FA-GQBN synthesis to determine the particle size. The GQD synthesis was already optimized, with a size range of 2 to 6 nm (Figure 8a), but once conjugated to hBN and FA, the nanoassemblies showed significant size variations. Multiple trials were performed to optimize the size.

The original conjugation protocol produced particles too large for DLS measurement. After adjusting the protocols based on DLS results, the EDC/NHS amount and folic acid concentrations were adjusted, reaction times were shortened, and sonication and filtration were incorporated to improve size. Filtration led to better size distributions, though filtration resulted in folic acid loss, as confirmed by FTIR analysis (as shown in Figure 7f).

DLS characterizations of FA-GQBN samples, measured a day after synthesis, showed improvements in size distribution, indicating that reducing EDC/NHS and optimizing reaction time played a role in reducing size. However, a significant issue arose when samples were left in storage. Later batches of FA-GQBN, which were stored at 4°C for one week before DLS analysis, showed substantial aggregation, with size distributions shifting to 500–1000 nm. This indicates that prolonged storage may promote nanoparticle clustering, possibly due to insufficient stabilization or the formation of aggregates over time.

To address this issue, PEGylation was done using amine-terminated PEG with a molecular weight of 2000 Da as a stabilization strategy to improve colloidal stability and prevent aggregation. The hBN powder size is 150 to 250 nm, and GQBN is 200 to 600 nm. There is a size reduction to 10 to 30 nm in PEG-GQBN (Figure 8g) due to surface functionalization with PEG, which improves

dispersion and reduces aggregation. Free FA has a size range of 200 to 400 nm. The conjugation to PEG-GQBN prevents a significant size increase by limiting the aggregation through steric stabilization. As a result, FA-PEG-GQBN remained under 160 nm (Figure 8h), reflecting the combined effects of functionalization and improved dispersion.

The importance of fine-tuning reaction conditions, filtration methods, and surface modifications to achieve a stable FA-GQBN nanoassembly with a controlled size distribution was demonstrated throughout the iterative optimization process. Decreasing concentrations of EDC/NHS and reaction time with increased sonication minimized excessive aggregation while maintaining folic acid conjugation. PEGylation successfully improved colloidal stability, with PEG-GQBN achieving a size distribution of 10–30 nm. Incorporating folic acid onto PEG-GQBN maintained a size below 200 nm in trials, making the optimized FA-PEG-GQBN suitable for biomedical applications. Despite these improvements, there were still some variations in size, suggesting that further optimization may be necessary to achieve a consistently uniform nanoparticle size.

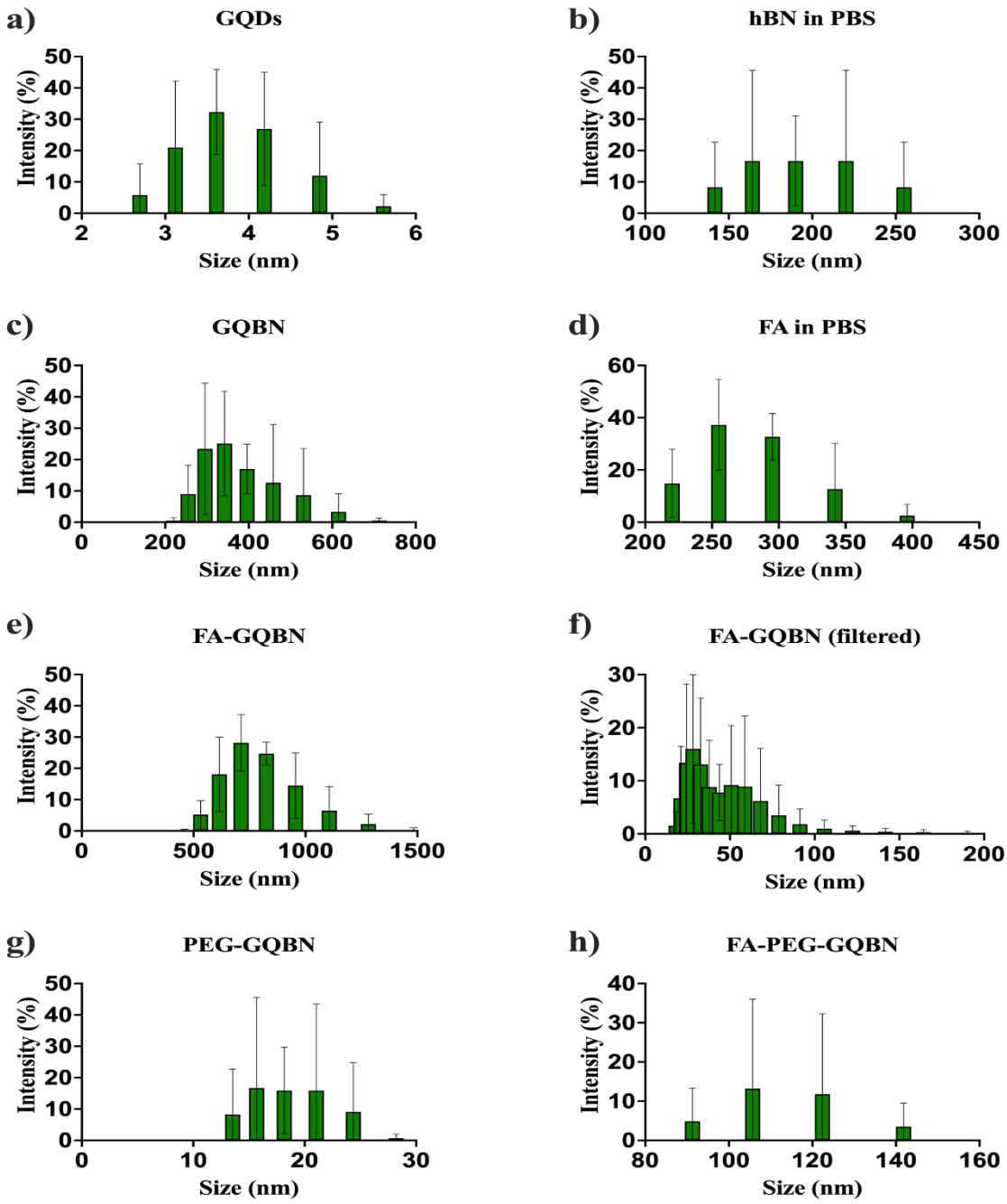

Figure 8. *DLS data of a) GQDs, b) hBN in PBS, c) GQBN, d) FA in PBS, e) FA-GQBN, f) filtered FA-GQBN, g) PEG-GQBN, h) FA-PEG-GQBN. Data are presented as mean ± SD (n=3).*

TEM Imaging

TEM was used to examine the morphology of the synthesized GQBN. Figure 9 shows the TEM images of the GQBN nanocomposites. As shown in Figure 9a and Figure 9b, the nanoparticles are predominantly spherical particles, with GQDs visible as darker contrast spots embedded within the lighter hBN. Figure 9c confirms denser aggregates forming, where the individual GQDs remain visible within the hBN. The clustering of the nanoparticles can also be seen. These TEM findings agree with the DLS data seen in Figure 8. In Figure 9d, the particles appear more aggregated, forming loosely bound clusters while still maintaining nanoscale dimensions. Across all images, the particles remain below 50 nm in size. The contrast differences observed in the TEM images suggest the successful integration of GQDs onto the hBN surface, forming the desired nanocomposite.

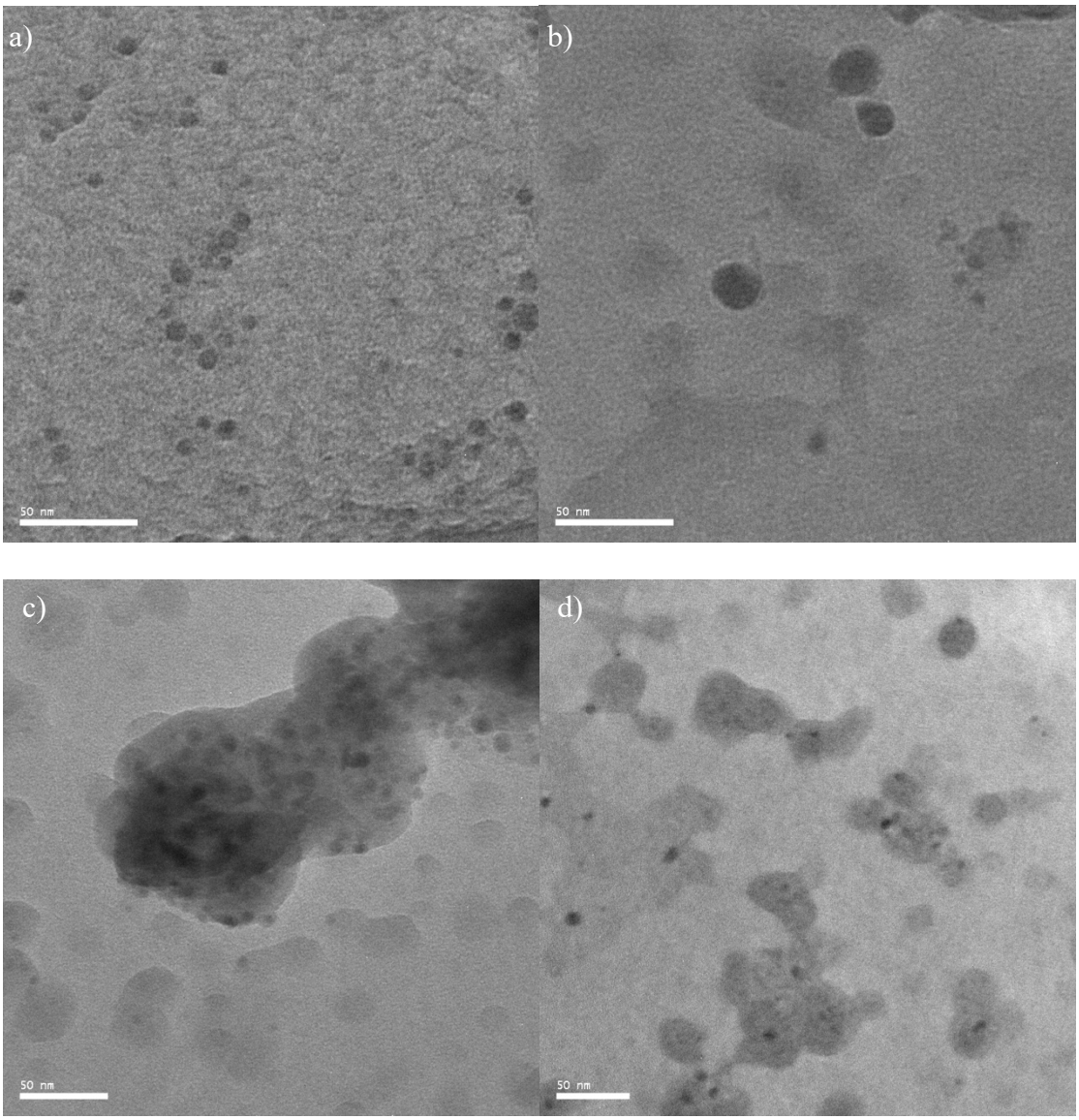

Figure 9. *TEM images of GQBN in a) 80k, b) 80k, c) 60k, and d) 50k magnification with 50 nm size bars.*

Confocal Imaging

Confocal laser scanning microscopy was used to examine the cellular uptake and localization of GQDs and FA-GQBN nanocomposites in A549 lung cancer cells, as HEC1A cells were unavailable when imaging. Figure 10a to Figure 10b shows GQD-treated cells with varying magnifications and scale bars. Figure 10a is a zoomed-in image of Figure 10b. Figure 10c shows

FA-GQBN-treated cells. The images have distinct red fluorescence signals distributed throughout the cytoplasm, suggesting internalization of GQDs. The black spherical structures visible in the images represent the cell nuclei. This confirms that the red fluorescence is from the GQDs. Compared to GQDs alone, FA-GQBN-treated cells exhibit a more localized fluorescence intensity, particularly near the nucleus, indicating enhanced uptake likely due to folate receptor-mediated endocytosis. These findings demonstrate the potential targeting capability of FA-functionalized nanocomposites for application in cancer-specific delivery.

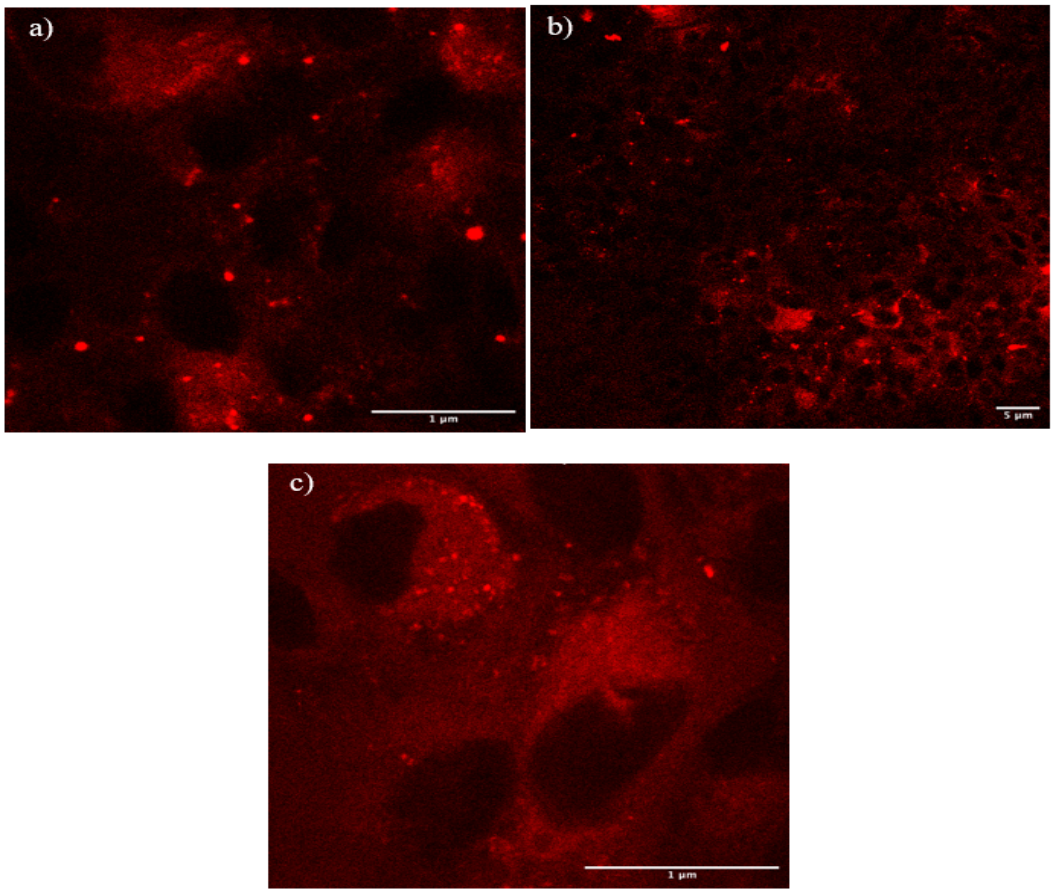

Figure 10. *Confocal laser scanning microscopy images of A549 cells with a.) GQDs with a scale bar of 1µm, b.) GQDs with a scale bar of 5 µm, and c.) FA-GQBN with a scale bar of 1µm.*

XTT Cell Viability

The biocompatibility of the GQDs, GQBN, PEG-GQBN, and FA-PEG-GQBN at a concentration of 100 μg/mL was evaluated using an XTT assay with 3-hour and 24-hour incubation periods with HEC1A cells. At the 3-hour time point (Figure 11a), a significant increase of 20.2% in cell viability was observed with GQD treatment. This was even more pronounced at 24 hours (Figure 11b), where GQDs resulted in a 106.7% increase. This suggests that the GQDs may enhance cellular metabolic activity and proliferation[28]. The cell viability decreased with the PEG-GQBN at both the 3-hour and 24-hour time points (Figure 11a and b, respectively), despite PEG being known for its biocompatibility. This reduction may be due to incomplete removal of EDC/NHS coupling agents during the synthesis, resulting in residual cytotoxicity. At the 24-hour time point (Figure 11b), trends were noticeable even though no statistically significant differences in viability were observed between the groups. Both GQDs and GQBN showed increases in cell viability compared to the control. FA-PEG-GQBN exhibited higher cell viability than PEG-GQBN, possibly because of the additional dialysis step during the folic acid conjugation reaction that removed residual EDC/NHS coupling agents. These results suggest that GQDs and GQBN are not only biocompatible but may also promote cell viability over time. It also suggests that FA-functionalization can mitigate the cytotoxic effects potentially introduced during PEG-GQBN synthesis.

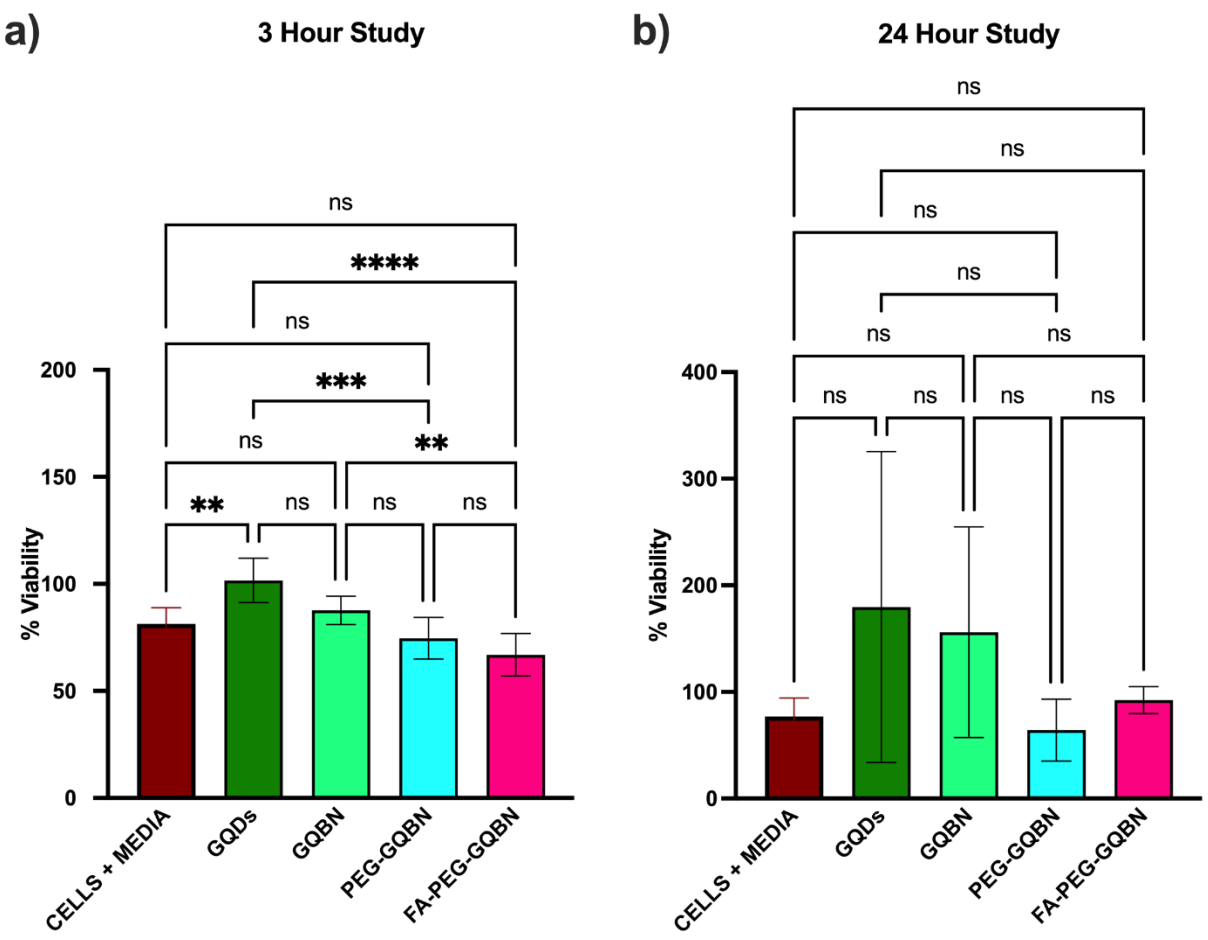

Figure 11. *In vitro XTT assay of relative cell viability of HEC1A cells incubated with media, GQDs, GQBN, PEG-GQBN, and FA-PEG-GQBN for a) 3 hours and b) 24 hours. The concentration for all nanoparticles was 100 μg/mL. Data are presented as mean ± SD. Relative cell viabilities were normalized to the blank samples of media only. Error bars were based on the SD of six independently prepared samples under identical conditions. One-way ANOVA calculated P-values: ns=not significant, **p<0.01, ***p<0.001, ****p<0.0001 (n=6).*

LDH Release

An LDH assay was conducted to evaluate the membrane-damaging cytotoxicity of the GQDs and FA-PEG-GQBN in HEC1A cells following treatment with increasing concentration

(1–200 μg/mL) of the nanoparticles. LDH was specifically chosen for this study because ROS generated during PDT can damage cell membranes and lead to LDH release into the extracellular environment[50,51]. Therefore, this assay provides a way to indirectly assess whether laser-irradiated GQDs or FA-PEG-GQBN nanocomposites are producing ROS that is capable of damaging the cell membrane.

For GQDs (Figure 12a), no statistically significant differences were observed ($p > 0.05$). However, a subtle upward trend in cytotoxicity was noted with increasing concentration following laser exposure. This suggests a possible dose-dependent effect that could become more pronounced under optimized PDT conditions. These preliminary results imply that GQDs may begin to generate ROS at higher concentrations when irradiated. Still, the current laser parameters (785 nm, 15 seconds per well) may not be sufficient to induce substantial membrane damage. Similarly, FA-PEG-GQBN nanocomposites (Figure 12b) exhibited low cytotoxicity across all concentrations, with a slight increase in LDH release observed under laser treatment compared to non-treated controls, though again not statistically significant. An unexpected spike in LDH release was observed at two μg/mL in the non-irradiated group, representing experimental variability. This trend suggests that ROS production may occur, but not at a high enough level to cause detectable membrane damage under current experimental conditions.

The LDH assay indicates that GQDs and FA-PEG-GQBN nanocomposites do not induce substantial membrane damage under the current experimental conditions. However, subtle trends in laser-induced cytotoxicity support the hypothesis that these nanomaterials may generate ROS, and that further PDT optimization could improve their therapeutic performance.

Since there was an upward trend in percent cytotoxicity when irradiated for 15 seconds per well, laser irradiation, the exposure time was extended to 45 seconds per well. Another LDH assay

was performed to evaluate whether longer irradiation would enhance ROS generation and result in more membrane damage detectable by LDH release. While it was anticipated that exposing the cells to a longer irradiation time would amplify cytotoxic effects, the 45-second LDH data did not show a consistent increase across concentrations. For GQDs (Figure 13a), a statistically significant increase in cytotoxicity was only observed at five μg/mL for the non-laser-treated group. There was no increase in cytotoxicity with increasing concentrations. Similarly, FA-PEG-GQBN nanocomposites (Figure 13b) significantly increased at 100 μg/mL for the non-laser-treated group. Overall, the results remain inconclusive.

In this study, neither the synthesized GQDs nor the FA-PEG-GQBN nanoassemblies demonstrated significant ROS generation under light irradiation. Literature suggests that the ROS-producing capabilities of GQDs are highly dependent on their surface chemistry, particularly the presence of electron-donating or withdrawing functional groups[52]. Studies have shown that GQDs with high radical scavenging activity, such as thiourea-functionalized GQDs, tend to quench ROS rather than generate them, suppressing photodynamic effects[52]. Given these findings, the GQDs used in this work may limit ROS accumulation during laser irradiation. Incorporating PEG and FA in the FA-PEG-GQBN nanoassemblies may have further influenced surface interactions contributing to reduced ROS production.

Beyond material properties, experimental factors may have also contributed to the lack of observed ROS activity. The wavelength, intensity, or exposure time of the laser used may have been insufficient to activate the ROS effectively. The absence of beam-focusing optics could have led to dispersed laser delivery, resulting in lower laser intensity reaching the cells. Potential laser scattering by culture media on the cells may have further reduced the laser reaching the cells.

Any of these factors could have contributed to the limited ROS generation observed. Future studies could focus on optimizing the surface functionalization of GQDs to enhance π-electron density and ROS production and refining irradiation parameters and optical delivery systems to ensure effective activation during laser irradiation.

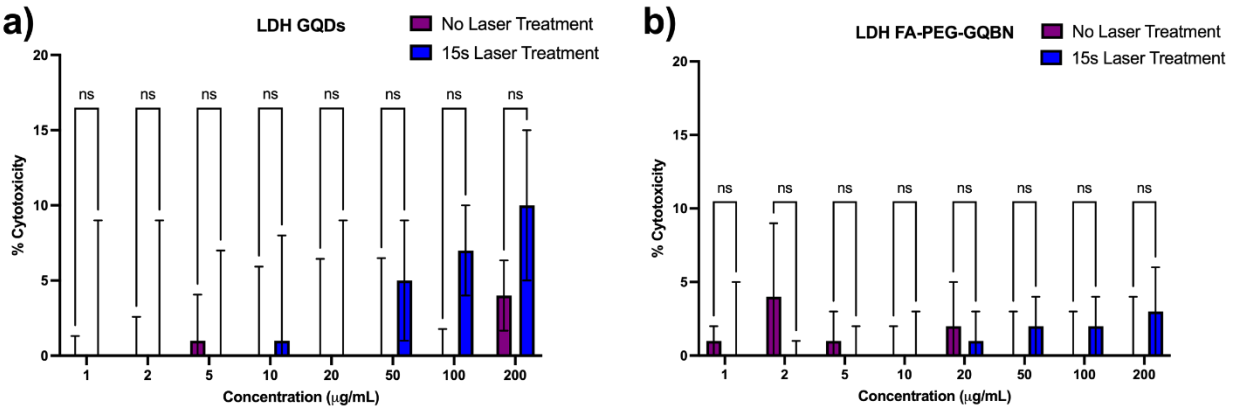

Figure 12. *In vitro LDH cytotoxicity assay of HEC1A cells treated with a) GQDs and b) FA-PEG-GQBNs, both at concentrations ranging from 1–200 μg/mL with and without 15 seconds per well of 785 nm laser irradiation. Data are presented as mean ± SD. Percent cytotoxicity was normalized to spontaneous LDH release and maximum LDH release. Error bars were based on the SD of six independently prepared samples under identical conditions. Two-way ANOVA calculated P-values: ns = not significant ($p > 0.05$, $n = 6$).*

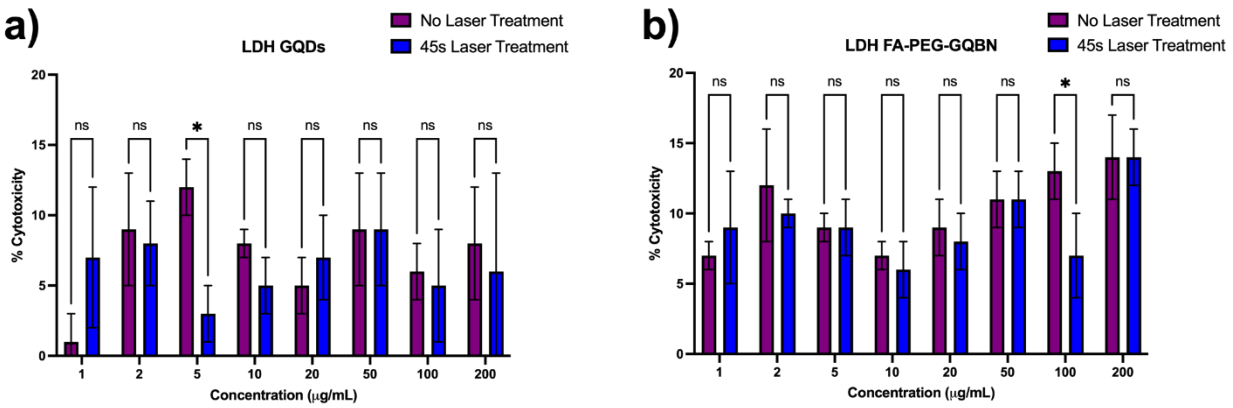

Figure 13. *In vitro LDH cytotoxicity assay of HEC1A cells treated with a) GQDs and b) FA-PEG-GQBNs, both at concentrations ranging from 1–200 μg/mL, with and without 45 seconds per well of 785 nm laser irradiation. Percent cytotoxicity was normalized to spontaneous and maximum LDH release. Data are presented as mean ± SD (n = 3). Error bars represent the standard deviation of three independently prepared samples under identical conditions. Statistical analysis was performed using two-way ANOVA: *p<0.05 and ns = not significant (p > 0.05).*

Future Direction: Biodistribution Study

The purpose of the *in vivo* study was to evaluate the biodistribution of PEG-GQBN and FA-PEG-GQBN nanocomposites in a murine model of endometrial cancer. By using the inherent fluorescence of GQDs, the distribution and tumor accumulation of both targeted and non-targeted nanomaterials over time can be tracked using IVIS Spectrum CT imaging. Subcutaneous tumors were successfully established in all Balb/c nude mice following injection with HEC1A cells. Both PEG-GQBN and FA-PEG-GQBN were administered via tail vein injection at a dose of 15 mg/kg, and imaging was performed at 1-, 4-, and 24-hours post-injection. The one and 24-hour timepoints were done using transillumination FLIT-CT to capture the 3D fluorescence (Figure 14), and epi-illumination 2D fluorescence imaging was done at the 4-hour mark (Figure 15). Despite these

efforts, no detectable fluorescence signal was observed at any time point for either PEG-GQBN or FA-PEG-GQBN. During the 4-hour imaging (Figure 15), widespread background autofluorescence was observed across both mice. This signal is commonly associated with dietary components, as standard rodent chow can contain chlorophyll (alfalfa), which exhibits strong autofluorescence[53]. This could be masking the signals associated with the nanoassemblies. These findings also indicate that the fluorescence of the GQDs was inadequate for *in vivo* detection under the selected excitation (405 nm) and emission (525 nm) wavelengths. Low photoluminescence of the GQDs or poor tissue penetration could contribute to this.

Future studies should focus on determining detection limits and optimizing excitation/emission settings by imaging known concentrations of PEG-GQBN and FA-PEG-GQBN. *Ex vivo* organ imaging could be performed to gain more insight into the biodistribution and nanoassembly accumulation. Organ homogenization followed by fluorescence imaging would help quantify nanoparticle fluorescence. Another future study that could be done is a histological analysis to visualize nanoparticle localization at the cellular level using H&E staining. While fluorescence-based biodistribution was not achieved, these results offer guidance for optimizing the biodistribution methods in future research.

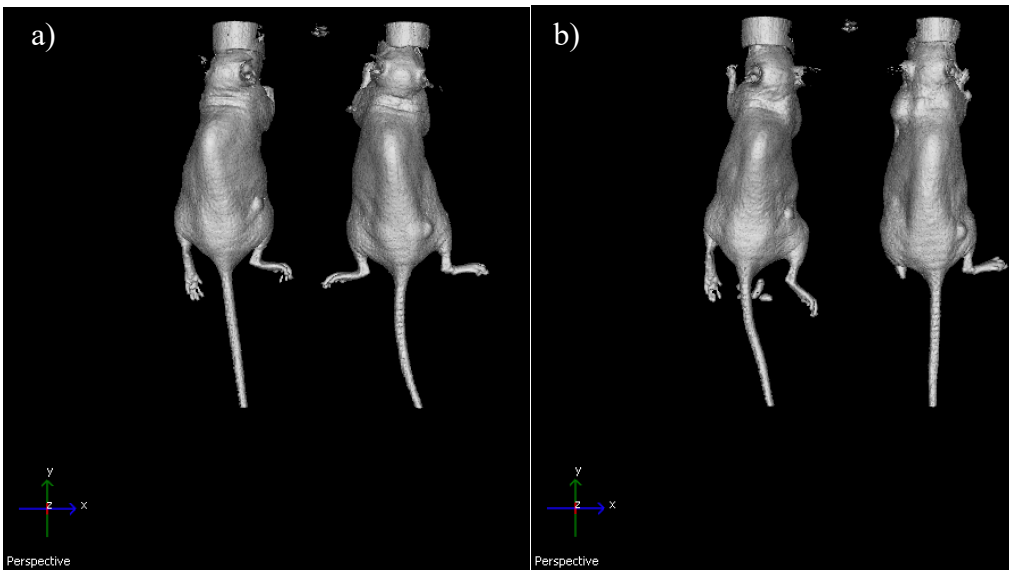

Figure 14. *In vivo biodistribution of Balb/c nude mice bearing HEC1A tumors on the right flank following intravenous administration of PEG-GQBN (left mouse) and FA-PEG-GQBN (right mouse) nanoassemblies. Transillumination FLIT-CT imaging was performed at a) 1 hour and b) 24 hours post-injection using an excitation wavelength at 405 nm and emission at 525 nm.*

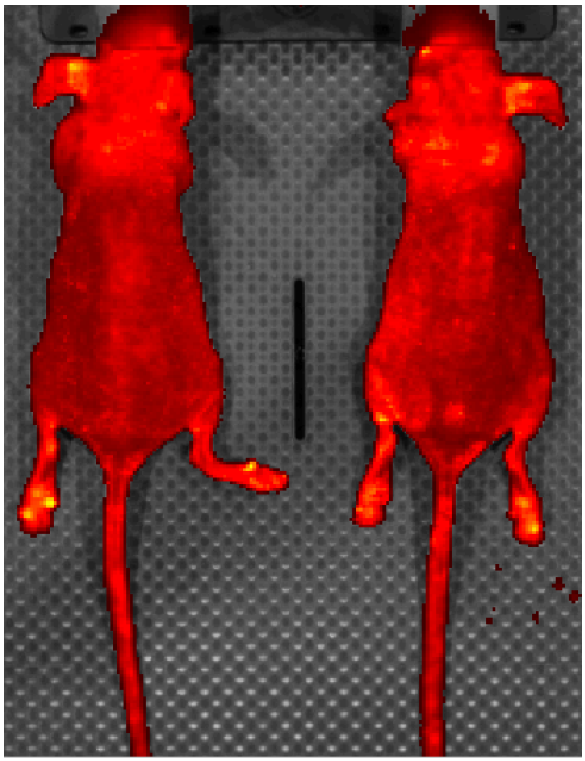

Figure 15. *In vivo biodistribution imaging of Balb/c nude mice bearing HEC1A tumors on the right flank following intravenous administration of PEG-GQBN (left mouse) and FA-PEG-GQBN (right mouse) nanoassemblies. Epi-illumination fluorescence imaging was performed at 4 hours post-injection using an excitation wavelength of 405 nm and emission at 525 nm.*

Chapter 5: Conclusion

This work presented the development and initial evaluation of a novel FA-PEG-GQBN nanocomposite for targeted PDT of endometrial cancer. GQDs were synthesized via a green synthesis approach using rice grains and embedded onto hBN to improve GQD stability. PEGylation was used to reduce aggregation and improve biocompatibility, while FA conjugation aimed to promote specific targeting to folate receptor-overexpressing endometrial cancer cells.

FTIR, DLS, TEM, and confocal microscopy characterization confirmed successful synthesis and functionalization of the FA-PEG-GQBN nanocomposites. FTIR spectra validated chemical modifications through characteristic peaks (–OH, C=O, C–O, and B–N) and peak shifts, specifically the 1390 cm^{-1} B–N band upon FA conjugation. This indicates the interaction between components of the nanoassembly. Filtration was observed to remove FA peaks. DLS analysis showed that GQDs exhibited a stable and narrow size distribution (2–6 nm), while GQBN composites showed significant aggregation (500–1000 nm) when stored. PEGylation reduced this aggregation, resulting in a more uniform size distribution, although FA conjugation led to a slight increase in particle size. TEM imaging further confirmed the successful formation of GQBN nanocomposites, with GQDs appearing as nanoscale dark contrast dots embedded within hBN, with visible aggregation. Confocal microscopy showed that GQDs retained their intrinsic fluorescence after conjugation, and FA-GQBN demonstrated cellular localization, demonstrating potential for targeted imaging. Additional staining strategies could enhance future cellular studies.

Biocompatibility and photodynamic potential were assessed using XTT and LDH assays in HEC1A cells. GQDs and GQBN were largely biocompatible, with GQDs promoting cell proliferation. However, PEG-GQBN showed some cytotoxicity, likely due to residual reactants (EDC/NHS) or PEG concentration. LDH assays showed slight increases in LDH release with

increasing concentrations of GQDs and FA-PEG-GQBN with 15s laser exposure, suggesting limited ROS generation. The 15-second laser exposure was likely insufficient to trigger the full extent of ROS generation. 45-second irradiation resulted in laser and no laser-treated GQDs and FA-PEG-GQBN groups showing LDH release. Conclusive evidence of ROS activity was not observed.

Preliminary *in vivo* biodistribution studies successfully established tumor-bearing mouse models without observed signs of toxicity or distress. However, no fluorescence signal was detected, and FA-targeting did not enhance signal localization. This indicates the need for further optimization of *in vivo* imaging sensitivity and nanoparticle design.

Initial results are promising, but further work needs to be done to fully understand and optimize the therapeutic efficacy of the FA-PEG-GQBN platform. Future directions include performing Singlet Oxygen Sensor Green (SOSG) assays to detect and quantify singlet oxygen generation directly, confirming type II ROS production. Flow cytometry could determine the specific modes of cell death induced by the laser treatment on the FA-PEG-GQBN, identifying whether the cells are dying via apoptosis or necrosis. To assess the efficacy of folic acid-mediated targeting, further confocal fluorescence imaging could be performed using both folate receptor-positive and receptor-negative cell lines, and the receptors could be blocked with free folic acid. Comparative *in vivo* analysis of PEG-GQBN and FA-PEG-GQBN will be crucial in validating the biodistribution and targeting specificity.

In conclusion, the synthesis of FA-PEG-GQBN nanoassemblies offers a novel and promising platform for targeted, minimally invasive PDT in endometrial cancer. Although initial results show successful synthesis, cellular uptake, intrinsic fluorescence, and early indications of ROS generation, further optimization is necessary to improve photodynamic efficacy. Future work

may also explore improving ROS production, increasing fluorescence intensity for real-time imaging *in vivo*, and integrating drug-loading capabilities to develop a multifunctional theranostic platform. The use of green-synthesized GQDs supports sustainable and cost-effective nanomaterial production. Overall, this work contributes to the advancement of PDT and provides a framework for designing next-generation nanotherapeutics.

Bibliography

1. Endometrial Cancer Treatment - NCI. https://www.cancer.gov/types/uterine/patient/endometrial-treatment-pdq (2024).
2. Key Statistics for Endometrial Cancer | How Common Is Uterine Cancer? https://www.cancer.org/cancer/types/endometrial-cancer/about/key-statistics.html.
3. Setiawan, V. W. *et al.* Type I and II Endometrial Cancers: Have They Different Risk Factors? *J. Clin. Oncol.* **31**, 2607–2618 (2013).
4. Endometrial cancer - Symptoms and causes. *Mayo Clinic* https://www.mayoclinic.org/diseases-conditions/endometrial-cancer/symptoms-causes/syc-20352461.
5. Radiation Therapy Side Effects - NCI. https://www.cancer.gov/about-cancer/treatment/types/radiation-therapy/side-effects (2018).
6. cancer, C. C. S. / S. canadienne du. Side effects of chemotherapy. *Canadian Cancer Society* https://cancer.ca/en/treatments/treatment-types/chemotherapy/side-effects-of-chemotherapy (2024).
7. Żołyniak-Brzuchacz, A., Barnaś, E., Bartusik-Aebisher, D. & Aebisher, D. The Use of Photodynamic Therapy in the Treatment of Endometrial Cancer—A Review of the Literature. *Int. J. Mol. Sci.* **25**, 8772 (2024).
8. Correia-Barros, G. *et al.* Applications of Photodynamic Therapy in Endometrial Diseases. *Bioengineering* **9**, 226 (2022).
9. Photodynamic therapy - Mayo Clinic. https://www.mayoclinic.org/tests-procedures/photodynamic-therapy/about/pac-20385027.

10. Correia, J. H., Rodrigues, J. A., Pimenta, S., Dong, T. & Yang, Z. Photodynamic Therapy Review: Principles, Photosensitizers, Applications, and Future Directions. *Pharmaceutics* **13**, 1332 (2021).

11. Sai, D. L., Lee, J., Nguyen, D. L. & Kim, Y.-P. Tailoring photosensitive ROS for advanced photodynamic therapy. *Exp. Mol. Med.* **53**, 495–504 (2021).

12. Ding, H. *et al.* Photoactivation Switch from Type II to Type I Reactions by Electron-Rich Micelles for Improved Photodynamic Therapy of Cancer Cells Under Hypoxia. *J. Control. Release Off. J. Control. Release Soc.* **156**, 276–280 (2011).

13. Tavakkoli Yaraki, M., Liu, B. & Tan, Y. N. Emerging Strategies in Enhancing Singlet Oxygen Generation of Nano-Photosensitizers Toward Advanced Phototherapy. *Nano-Micro Lett.* **14**, 123 (2022).

14. Calixto, G. M. F., Bernegossi, J., De Freitas, L. M., Fontana, C. R. & Chorilli, M. Nanotechnology-Based Drug Delivery Systems for Photodynamic Therapy of Cancer: A Review. *Molecules* **21**, 342 (2016).

15. Yu, L. *et al.* Towards overcoming obstacles of type II photodynamic therapy: Endogenous production of light, photosensitizer, and oxygen. *Acta Pharm. Sin. B* **14**, 1111–1131 (2024).

16. Advances in Structural Modifications and Properties of Graphene Quantum Dots for Biomedical Applications | ACS Omega. https://pubs.acs.org/doi/10.1021/acsomega.2c08183.

17. Ghaffarkhah, A. *et al.* Synthesis, Applications, and Prospects of Graphene Quantum Dots: A Comprehensive Review. *Small* **18**, 2102683 (2022).

18. Biswas, M. C., Islam, M. T., Nandy, P. K. & Hossain, M. M. Graphene Quantum Dots (GQDs) for Bioimaging and Drug Delivery Applications: A Review. *ACS Mater. Lett.* **3**, 889–911 (2021).

19. Chong, Y. *et al.* The *in vitro* and *in vivo* toxicity of graphene quantum dots. *Biomaterials* **35**, 5041–5048 (2014).

20. PubChem. Graphene quantum dot. https://pubchem.ncbi.nlm.nih.gov/compound/146000141.

21. Sengupta, S. *et al.* A review on synthesis, toxicity profile and biomedical applications of graphene quantum dots (GQDs). *Inorganica Chim. Acta* **557**, 121677 (2023).

22. Zhao, C. *et al.* Synthesis of graphene quantum dots and their applications in drug delivery. *J. Nanobiotechnology* **18**, 142 (2020).

23. Bressi, V., Ferlazzo, A., Iannazzo, D. & Espro, C. Graphene Quantum Dots by Eco-Friendly Green Synthesis for Electrochemical Sensing: Recent Advances and Future Perspectives. *Nanomaterials* **11**, 1120 (2021).

24. Yan, C. *et al.* Highly biocompatible graphene quantum dots: green synthesis, toxicity comparison and fluorescence imaging. *J. Mater. Sci.* **55**, 1198–1215 (2020).

25. Cui, Y. *et al.* A Review of Advances in Graphene Quantum Dots: From Preparation and Modification Methods to Application. *C* **10**, 7 (2024).

26. Chung, S., Revia, R. A. & Zhang, M. Graphene Quantum Dots and Their Applications in Bioimaging, Biosensing, and Therapy. *Adv. Mater.* **33**, 1904362 (2021).

27. Wang, L. *et al.* Ultrastable Amine, Sulfo Cofunctionalized Graphene Quantum Dots with High Two-Photon Fluorescence for Cellular Imaging. *ACS Sustain. Chem. Eng.* **6**, 4711–4716 (2018).

28. Kumawat, M. K., Thakur, M., Gurung, R. B. & Srivastava, R. Graphene Quantum Dots for Cell Proliferation, Nucleus Imaging, and Photoluminescent Sensing Applications. *Sci. Rep.* **7**, 15858 (2017).

29. Kersting, D. *et al.* From in vitro to ex vivo: subcellular localization and uptake of graphene quantum dots into solid tumors. *Nanotechnology* **30**, 395101 (2019).

30. Ge, J. *et al.* A graphene quantum dot photodynamic therapy agent with high singlet oxygen generation. *Nat. Commun.* **5**, 4596 (2014).

31. Photothermal therapy using graphene quantum dots - PMC. https://www.ncbi.nlm.nih.gov/pmc/articles/PMC10444203/.

32. Detty, M. R., Gibson, S. L. & Wagner, S. J. Current Clinical and Preclinical Photosensitizers for Use in Photodynamic Therapy. *J. Med. Chem.* **47**, 3897–3915 (2004).

33. Peng, J. *et al.* Fabrication of graphene quantum dots and hexagonal boron nitride nanocomposites for fluorescent cell imaging. *J. Biomed. Nanotechnol.* **9**, 1679–1685 (2013).

34. Hu, Q. *et al.* Controllable synthesis and enhanced microwave absorption properities of novel lightweight graphene quantum dots/hexagonal boron nitride composites. *Carbon* **182**, 134–143 (2021).

35. Satawara, A. M., Shaikh, G. A., Gupta, S. K. & Gajjar, P. N. Structural, electronic and optical properties of hexagonal boron-nitride (h-BN) monolayer: An Ab-initio study. *Mater. Today Proc.* **47**, 529–532 (2021).

36. Rasul, M. G., Kiziltas, A., Arfaei, B. & Shahbazian-Yassar, R. 2D boron nitride nanosheets for polymer composite materials. *Npj 2D Mater. Appl.* **5**, 1–18 (2021).

37. Roy, S. *et al.* Structure, Properties and Applications of Two-Dimensional Hexagonal Boron Nitride. *Adv. Mater.* **33**, 2101589 (2021).

38. Chen, D. *et al.* Sub-10 nm stable graphene quantum dots embedded in hexagonal boron nitride. *Nanoscale* **11**, 4226–4230 (2019).

39. Sharker, S. M. Hexagonal Boron Nitrides (White Graphene): A Promising Method for Cancer Drug Delivery. *Int. J. Nanomedicine* **14**, 9983–9993 (2019).

40. Boron nitride. *American Chemical Society* https://www.acs.org/molecule-of-the-week/archive/b/boron-nitride.html.

41. Zwicke, G. L., Mansoori, G. A. & Jeffery, C. J. Utilizing the folate receptor for active targeting of cancer nanotherapeutics. *Nano Rev.* **3**, 10.3402/nano.v3i0.18496 (2012).

42. Scaranti, M., Cojocaru, E., Banerjee, S. & Banerji, U. Exploiting the folate receptor α in oncology. *Nat. Rev. Clin. Oncol.* **17**, 349–359 (2020).

43. Senol, S. *et al.* Folate receptor α expression and significance in endometrioid endometrium carcinoma and endometrial hyperplasia. *Int. J. Clin. Exp. Pathol.* **8**, 5633–5641 (2015).

44. Wang, X. *et al.* Multifunctional graphene quantum dots for simultaneous targeted cellular imaging and drug delivery. *Colloids Surf. B Biointerfaces* **122**, 638–644 (2014).

45. Feng, S. *et al.* Folate-conjugated boron nitride nanospheres for targeted delivery of anticancer drugs. *Int. J. Nanomedicine* **11**, 4573–4582 (2016).

46. Pareek, A., Kumar, D., Pareek, A. & Gupta, M. M. Advancing Cancer Therapy with Quantum Dots and Other Nanostructures: A Review of Drug Delivery Innovations, Applications, and Challenges. *Cancers* **17**, 878 (2025).

47. Boidin, L. *et al.* Targeted Photodynamic Therapy using a Vectorized Photosensitizer coupled to Folic Acid Analog induces Ovarian Tumor Cell Death and inhibits IL-6-mediated Inflammation. *J. Controlled Release* **371**, 351–370 (2024).

48. Kalita, H. *et al.* Efficient synthesis of rice based graphene quantum dots and their fluorescent properties. *RSC Adv.* **6**, 23518–23524 (2016).

49. Fabrication and Characterization of Electrospun Folic Acid/Hybrid Fibers: In Vitro Controlled Release Study and Cytocompatibility Assays. https://www.mdpi.com/2073-4360/13/20/3594.

50. Recent advances in reactive oxygen species (ROS)-responsive drug delivery systems for photodynamic therapy of cancer - PMC. https://pmc.ncbi.nlm.nih.gov/articles/PMC11725102/.

51. Reagen, S. *et al.* Development of Biodegradable GQDs-hMSNs for Fluorescence Imaging and Dual Cancer Treatment via Photodynamic Therapy and Drug Delivery. *Int. J. Mol. Sci.* **23**, 14931 (2022).

52. Jovanović, S. P. *et al.* Graphene quantum dots as singlet oxygen producer or radical quencher - The matter of functionalization with urea/thiourea. *Mater. Sci. Eng. C* **109**, 110539 (2020).

53. AutoFluores_brochure_NOchecker_web.pdf.